IJSSD Symposium on Progress in
STRUCTURAL STABILITY AND DYNAMICS
Lisbon, Portugal, July 22-24, 2015

THE DISCRETE PLANAR COSSERAT ROD AND ITS STABILITY ANALYSIS

Attila Kocsis

Department of Structural Mechanics, Budapest University of Technology and Economics, Hungary
e-mail: kocsis@ep-mech.me.bme.hu

Keywords: Cosserat rod, discrete model, buckling, stability, shear deformation.

Abstract. *In this paper a discrete model of the planar Cosserat rod is studied. The equilibrium equations, the stability matrix, and the buckling loads of the model are presented in a dimensionless form for axial loading, pinned ends, and linear elasticity. Numerical simulations are accomplished and bifurcation diagrams of a short chain are shown for large displacements and various stiffness values.*

1 INTRODUCTION

There is a wide range of available continuum rod models, starting from the planar *Bernoulli-Euler* and *Timoshenko* beams [1] to spatial *Kirchhoff* and *Cosserat* rods [2]. These models have a vast range of applications, but their equilibrium states can only be obtained analytically for special loading and boundary conditions. Otherwise, mathematical discretization of the governing equations, or a discrete counterpart of the continuum model are needed, and numerical simulations can be accomplished. Discrete models can be more advantageous than continuum ones if, for instance, the rod–like structure has varying stiffness and/or geometric properties along the length. But discrete models are also used in modelling macromolecules [3] or nanobeams [4]. Several discrete models have already been introduced. For example, *Hencky*'s chain [5] is the discrete version of the *Bernoulli-Euler* beam, the elastic web of links [6] is the discrete model of the unbendable, inextensible, but shearable beam of *Timoshenko* [1], while the bielastic web of links [7] is the discrete version of *Csonka*'s beam [8], or the spatial stack–of–plate model of *Coleman* et al [3] is the discrete counterpart of the general *Cosserat* rod.

Recently, a discrete model of the planar *Cosserat* rod has been developed [9], and its analytical buckling analysis has been accomplished for pinned ends and axial loading. In this paper we study this model in more detail. In Section 2 the model, its governing equations and buckling loads are reviewed based on [9]. In Section 3 the equilibrium states of a short chain are computed for large displacements with the Simplex Scanning Algorithm [10], implementing qualitatively different material properties. Bifurcations diagrams are shown and the obtained results are thoroughly discussed. Finally, conclusions are drawn in Section 4.

2 THE MECHANICAL MODEL

Figure 1 shows the studied model. There are N+1 elastically connected rigid plates. Plate 1 is attached to a fixed hinge, while plate N+1 is loaded by a horizontal force P. A global basis is fixed by the orthonormal vectors $\mathbf{e}_1$ and $\mathbf{e}_2$, along which the coordinates are denoted by X and Y, respectively. The centroid of plate n is given by vector $\mathbf{x}^n$, the angle of the plate from the X-axis is denoted by α^n. The relative translation of plate n+1 with respect to plate n is $\mathbf{r}^n = \mathbf{x}^{n+1} - \mathbf{x}^n$.

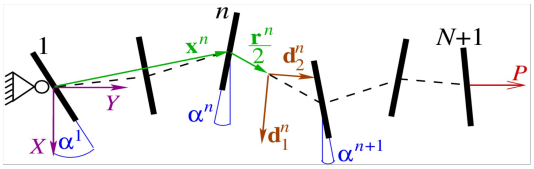

Figure 1: The mechanical model under tensile load.

A material frame is defined for each segment of the chain by a local coordinate system, fixed at the mid point of $\mathbf{r}^n$ and spanned by the right–handed orthonormal vectors $\mathbf{d}^n_1$ and $\mathbf{d}^n_2$. These vectors are stored in matrix $\mathbf{B}^n=[\mathbf{d}^n_1\ \mathbf{d}^n_2]$. The angle of $\mathbf{d}^n_1$ from the X-axis is the arithmetic mean of the angles α^{n+1} and α^n, hence

$$\mathbf{B}^n = \begin{bmatrix} \cos\left((\alpha^{n+1}+\alpha^n)/2\right) & -\sin\left((\alpha^{n+1}+\alpha^n)/2\right) \\ \sin\left((\alpha^{n+1}+\alpha^n)/2\right) & \cos\left((\alpha^{n+1}+\alpha^n)/2\right) \end{bmatrix}.$$

The components of the relative translation $\mathbf{r}^n$ with respect to the material frame is collected in $\boldsymbol{\rho}^n$, i.e. $\mathbf{r}^n=\mathbf{B}^n\boldsymbol{\rho}^n$.

2.1 Potential energy, equilibrium equations and the stability matrix

In the rest position, the plate rotations are $\bar{\alpha}$ and the relative translations are $\bar{\boldsymbol{\rho}}=[\bar{\rho}_1\ \bar{\rho}_2]^T$. Upon loading, segment n may undergo bending and translational deformation, $\Delta\alpha^n=\alpha^{n+1}-\alpha^n$ and $\Delta\boldsymbol{\rho}^n=\boldsymbol{\rho}^n-\bar{\boldsymbol{\rho}}$, respectively. Here $\Delta\rho^n_1$ is the shear deformation and $\Delta\rho^n_2$ is the normal deformation. The shear deformation of the model is area preserving, following the large shear theory of *Love* [11]. Each segment of the studied structure has the same bending, shear and normal stiffness, which are denoted by $EI/|\bar{\boldsymbol{\rho}}|$, $GA_0/|\bar{\boldsymbol{\rho}}|$ and $EA/|\bar{\boldsymbol{\rho}}|$, respectively. According to [9], the following parameters can be introduced:

$$s=\frac{GA_0}{S},\quad q=\frac{EA}{S}. \tag{1}$$

Here s and q are the dimensionless shear and normal stiffness, respectively, and

$$S=\frac{EI}{|\bar{\boldsymbol{\rho}}|^2}+GA_0+EA.$$

The dimensionless bending stiffness hence $EI/S/|\bar{\boldsymbol{\rho}}|^2=1-s-q$.

With the above notations the dimensionless strain energy of the linear elastic chain is:

$$\psi=\frac{1}{2}\sum_{n=1}^{N}\left\{(1-s-q)\left(\alpha^{n+1}-\alpha^n\right)^2+(\boldsymbol{\varepsilon}^n)^T\mathbf{H}\boldsymbol{\varepsilon}^n\right\}. \tag{2}$$

Here $\mathbf{H}$ is the dimensionless translational stiffness matrix (with $H_{11}=s$, $H_{22}=q$), and $\boldsymbol{\varepsilon}^n=\Delta\boldsymbol{\rho}^n/|\bar{\boldsymbol{\rho}}|$. The potential energy of the time–independent tensile force is:

$$\Pi=-\frac{\lambda}{|\bar{\boldsymbol{\rho}}|}\mathbf{e}_2^T\mathbf{x}^{N+1},$$

where $\lambda=P/S$ is the dimensionless load.

It is shown in [9] that

$$\boldsymbol{\varepsilon}^n = \lambda \mathbf{H}^{-1} (\mathbf{B}^n)^T \mathbf{e}_2, \tag{3}$$

which implies that the total potential, $E=\psi+\Pi$, can be reduced to the following form:

$$E_{\mathrm{red}} = \frac{1}{2} \sum_{n=1}^{N} \left\{ (1-s-q)(\alpha^{n+1}-\alpha^n)^2 - \lambda \mathbf{e}_2^T \left(\lambda \mathbf{C}^n \mathbf{e}_2 + 2\bar{\mathbf{r}}_d^n \right) \right\}. \tag{4}$$

Here $\boldsymbol{C}^n=\mathbf{B}^n\mathbf{H}^{-1}(\mathbf{B}^n)^{\mathrm{T}}$ is the translational compliance matrix of segment n in the global reference frame, and $\bar{\mathbf{r}}^n{}_d=\mathbf{B}^n\bar{\boldsymbol{\rho}}/|\bar{\boldsymbol{\rho}}|$.

The partial derivative of (4) with respect to α^n gives the equilibrium equation of plate n:

$$(1-s-q)(-\alpha^{n+1}+2\alpha^n-\alpha^{n-1}) - \frac{\lambda^2}{2}\mathbf{e}_2^T \left(\mathbf{C}^n + \mathbf{C}^{n-1} \right) \mathbf{e}_1 - \frac{\lambda}{2}\mathbf{e}_1^T \left(\bar{\mathbf{r}}_d^n + \bar{\mathbf{r}}_d^{n-1} \right) = 0, \tag{5}$$

n=1,2,...,N, with boundary conditions $\alpha^0=\alpha^2$ and $\alpha^{N+2}=\alpha^N$ [9].

For buckling and stability analyses one has to compile the stability matrix $\mathbf{A}$, which is composed of the second partial derivatives of (4):

$$\begin{aligned} \frac{\partial^2 E_{\mathrm{red}}}{\partial\alpha^n \partial\alpha^n} &= 2(1-s-q) - \frac{\lambda^2}{4} \left\{ \mathbf{e}_1^T \left(\mathbf{C}^n + \mathbf{C}^{n-1} \right) \mathbf{e}_1 - \mathbf{e}_2^T \left(\mathbf{C}^n + \mathbf{C}^{n-1} \right) \mathbf{e}_2 \right\} \\ &\quad + \frac{\lambda}{4} \mathbf{e}_2^T \left(\bar{\mathbf{r}}_d^n + \bar{\mathbf{r}}_d^{n-1} \right), \\ \frac{\partial^2 E_{\mathrm{red}}}{\partial\alpha^n \partial\alpha^{n-1}} &= -(1-s-q) - \frac{\lambda^2}{4} \left(\mathbf{e}_1^T \mathbf{C}^{n-1} \mathbf{e}_1 - \mathbf{e}_2^T \mathbf{C}^{n-1} \mathbf{e}_2 \right) + \frac{\lambda}{4} \mathbf{e}_2^T \bar{\mathbf{r}}_d^{n-1}. \end{aligned}$$

It is worth mentioning that the top plate could also be supported by a roller against translation along the X-axis. It would be more reasonable in a structural engineering point of view. However, the structure would possess the same equilibrium configurations with such a roller as without it. Only a free rigid–body–like rotation would disappear. Besides, the application of a roller could affect the stability of the equilibrium states: Stability could be gained for some unstable equilibrium states with the roller. We will show examples for it in our numerical analysis.

2.2 Buckling

In a straight rest position, $\bar{\alpha}=0$ and $\bar{\mathbf{r}}^n{}_d=[0\ 1]^{\mathrm{T}}$, the equilibrium equations are fulfilled by $\alpha^n=0$, and λ is arbitrary. In this case a *Haringx*-type formula can be obtained for the critical load parameters [9]:

$$\lambda_{2k,2k+1}^{\mathrm{cr}} = \frac{q\ s}{2(q-s)} \left(1 \pm \sqrt{1 + 16(1-s-q)\frac{q-s}{q\ s} \cdot \frac{1-\cos(k\pi/N)}{1+\cos(k\pi/N)}} \right), \tag{6}$$

k=0,1,...,N-1. We note that $\lambda^{\mathrm{cr}}{}_0=0$ belongs to the free rigid-body-like rotation of the unloaded chain, which is not a buckling load, while $\lambda^{\mathrm{cr}}{}_1=q\ s/(q\text{-}s)$ is a pure shear buckling mode. The other critical loads ($k > 0$) belong to buckling modes of mixed deformations.

In terms of the real stiffness values of the structure, the fundamental (compressive) critical force of the flexural, shearable, and extensible discrete *Cosserat* rod is:

$$P_{\mathrm{disc}}^{\mathrm{cr}} = \frac{GA_0}{2}\frac{EA}{EA-GA_0}\left(1-\sqrt{1+16\frac{EI/|\overline{\boldsymbol{\rho}}|^2}{GA_0}\frac{EA-GA_0}{EA}\cdot\frac{1-\cos(\pi/N)}{1+\cos(\pi/N)}}\right). \quad (7)$$

If the column is inextensible, i.e. $EA\to\infty$, then the above formula yields:

$$P_{\mathrm{ie}}^{\mathrm{cr}} = \frac{GA_0}{2}\left(1-\sqrt{1+16\frac{EI/|\overline{\boldsymbol{\rho}}|^2}{GA_0}\cdot\frac{1-\cos(\pi/N)}{1+\cos(\pi/N)}}\right). \quad (8)$$

This is a *Haringx*–type formula for the buckling load of a bendable and shearable discrete rod. Note that an *Engesser*'s based approach is developed in [12]. If the rod is inextensible and unshearable, i.e. $EA\to\infty$ and $GA_0\to\infty$, then the buckling load is:

$$P_{\mathrm{ie,us}}^{\mathrm{cr}} = -4\frac{EI}{|\overline{\boldsymbol{\rho}}|^2}\cdot\frac{1-\cos(\pi/N)}{1+\cos(\pi/N)}. \quad (9)$$

Now we give the results of Eqs. (7)–(9) in the limit $|\overline{\boldsymbol{\rho}}|\to 0$ and $N\to\infty$ (while $|\overline{\boldsymbol{\rho}}|=l/N$, where l is the length of the rod). Eq. (9) yields the *Euler* formula,

$$P_{\mathrm{E}} = -\frac{\pi^2 EI}{l^2}, \quad (10)$$

Eq. (8) yields the *Haringx* formula [13],

$$P_{\mathrm{H}}^{\mathrm{cr}} = \frac{GA_0}{2}\left(1-\sqrt{1-4\frac{P_{\mathrm{E}}}{GA_0}}\right), \quad (11)$$

and Eq. (7) is a *Haringx*–type formula for the fundamental buckling load of a flexural, shearable, and extensible continuous (*Cosserat*) rod with pinned ends:

$$P_{\mathrm{cont}}^{\mathrm{cr}} = \frac{GA_0}{2}\cdot\frac{EA}{EA-GA_0}\left(1-\sqrt{1-4\frac{P_{\mathrm{E}}}{GA_0}\cdot\frac{EA-GA_0}{EA}}\right). \quad (12)$$

Note that the above force is negative in compression.

3 NUMERICAL ANALYSIS

In this section we will study the equilibrium states of a chain of three plates (N=2) for large displacements and different stiffness parameters. First we review the buckling loads of the chain based on previous analytical results, and choose stiffness parameters for the numerical study in an appropriate way. Then we describe the applied numerical procedure. Finally, we show and discuss the results of the numerical simulations.

3.1 The studied chains

The studied chain of three plates is straight in the rest position, its buckling loads are from (6) at N=2:

$$\lambda_1^{\mathrm{cr}} = \frac{q\ s}{q-s},$$

$$\lambda_{2,3}^{\mathrm{cr}} = \frac{q\ s}{2(q-s)}\left(1 \pm \sqrt{1+16(1-s-q)\frac{q-s}{q\ s}}\right). \tag{13}$$

Note that the solutions for (13) are complex if the sign of the discriminant d is negative. Hence, there are *at most* three buckling loads, and their signs depend on the ratio of q and s. If $s<q$, then λ^{cr}_1 is positive (which means pure shear buckling under tension), λ^{cr}_2 is positive, and λ^{cr}_3 is negative. If $s>q$, then all the buckling loads are negative (i.e. buckling occurs under compression only). Meanwhile, at the load level

$$\lambda_{\mathrm{comp}} = -q, \tag{14}$$

the straight chain is entirely compressed. Hence, increasing the load beyond λ_{comp} is not admissible physically, because then the plates should penetrate one another. Note that the pure shear buckling under compression is always physically inadmissible.

Now the plane of stiffness parameters, (s, q), is shown in Figure 2. The line $s+q=1$ separates the parameter plane into two triangles. Since $s+q>0$ must hold for a chain of positive bending stiffness, only the lower triangle is relevant. According to [9], this triangle can be divided into six parts. It is partitioned into three main parts by line $s=q$ (which separates chains with positive and negative pure shear buckling loads), and by curve $d=0$ (which separates real and complex roots of (13)). Then these three parts are divided further by curve $\lambda^{cr}_{2,3}=-q$, which separates physically admissible and inadmissible mixed buckling modes. Each of these six parts belongs to a chain of different buckling behavior. Sample points, denoted by I to VI, are placed in the partitions.

The coordinates, s and q, of these sample points, and the corresponding buckling loads are given in Table 1. Chains equipped with these stiffness properties are also numbered form I to VI. For Chain I, two tensile and one compressive buckling loads exist, and all of them are physically admissible. For Chain II, also two tensile and one compressive buckling loads exist, but the compressive load is not admissible physically, $\lambda^{cr}_3<-q$. For Chain III, there are three compressive buckling loads, and all of them are physically inadmissible. For Chain IV, there are three compressive buckling loads, and only λ^{cr}_3 is physically admissible. For Chain V, there are three compressive buckling loads, both λ^{cr}_2 and λ^{cr}_3 are physically admissible. For Chain VI, there is only a physically inadmissible pure shear buckling under compression.

3.2 Procedure of the numerical simulation

We will study six chains with stiffness parameters listed in Table 1. The equilibrium equations are (5) for N=2. Hence, there are three equations, which are dependent on the angular variables α^1, α^2, and α^3, and on the load parameter λ. Therefore, the solutions form *equilibrium paths*, which can be uniquely embedded in a four dimensional general representation space (GRS).

Since the equation system to solve is nonlinear, its roots are numerically approximated by using the *Simplex Scanning Algorithm* [10]. The studied domain of α^1, α^2 and α^3 is in $[-\pi/2, \pi/2]$, while that of λ is in [-10, 10]. The discretization in the corresponding directions are:

151x151x151x901. The result of the scanning process is then refined by the *Newton–Raphson Method*. Finally, the stability of the equilibrium states are determined based on the smallest eigenvalue of the stability matrix **A**, which is computed numerically for each configuration. All the above computations are coded in *Fortran 90*.

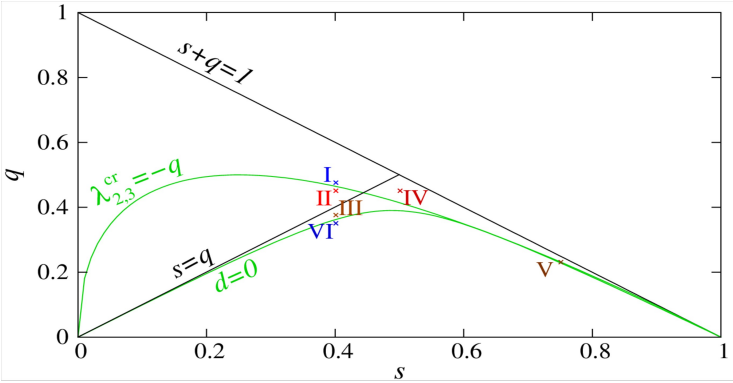

Figure 2: The plane of the stiffness parameters s and q. The part below $s+q=1$ is divided into six pieces by line $s=q$, and curves $d=0$ and $\lambda^{cr}_{2,3}=-q$. The studied six stiffness parameter pairs are represented by points I–VI, placed in the six distinct parts. See Table 1 for the coordinates of the denoted points and the corresponding buckling loads.

Table 1: Stiffness parameters of the studied chains and the corresponding buckling load parameters. Physically admissible buckling loads are bold.

Chain No.	q	s	λ^{cr}_1	λ^{cr}_2	λ^{cr}_3
I	0.475	0.400	**2.533**	**2.961**	**-0.428**
II	0.450	0.400	**3.600**	**4.124**	-0.524
III	0.375	0.400	-6.000	-4.897	-1.103
IV	0.450	0.500	-4.500	-4.290	**-0.210**
V	0.230	0.750	-0.332	**-0.197**	**-0.135**
VI	0.350	0.400	-2.800	-	-

3.3 Results

The resulting equilibrium paths are uniquely represented in the 4D GRS, which is not feasible to plot. Instead, we will show 2D and 3D projections of these paths. In the diagrams hereafter, blue and red colors denote stable and unstable equilibrium states, respectively, while green color denotes physically inadmissible states, where $\Delta\rho^1_2<-\bar{\rho}_2$ or $\Delta\rho^2_2<-\bar{\rho}_2$. The figures were made with *Gnuplot 4.6.4*.

We show the 2D projection of the paths onto the subspace (α^1, λ) for the studied six stiffness parameter pairs in Figure 3. These diagrams are discussed in the followings.

On the diagram for Chain I, three bifurcations of the trivial path (vertical line at $\alpha^1=0$) can be seen, where secondary paths evolve. These bifurcation points coincide with the analytical results, detailed in Table 1, which verifies the algorithm. Note that the trivial path is stable between $0<\lambda<\lambda^{cr}_1$. Under tension, there are two secondary paths, and only one of them is stable, the one that corresponds to pure shear buckling. It may be unusual that buckling under compression leads to an unstable secondary branch, but this is due to the lack of a roller at plate $N+1$. Applying such a roller would lead to the same paths, but some unstable states (the trivial path under compression up to the bifurcation, and the compressive secondary path, for example) would be stabilized. Not much beyond the compressive buckling load, the trivial equilibrium state becomes physically inadmissible. Note that the algorithm finds higher order branches, too.

The diagram for Chain II shows three bifurcations: two under tension and one under compression. Contrary to the previous case, here the buckling under compression is physically inadmissible. These findings also match the analytical results of Table 1.

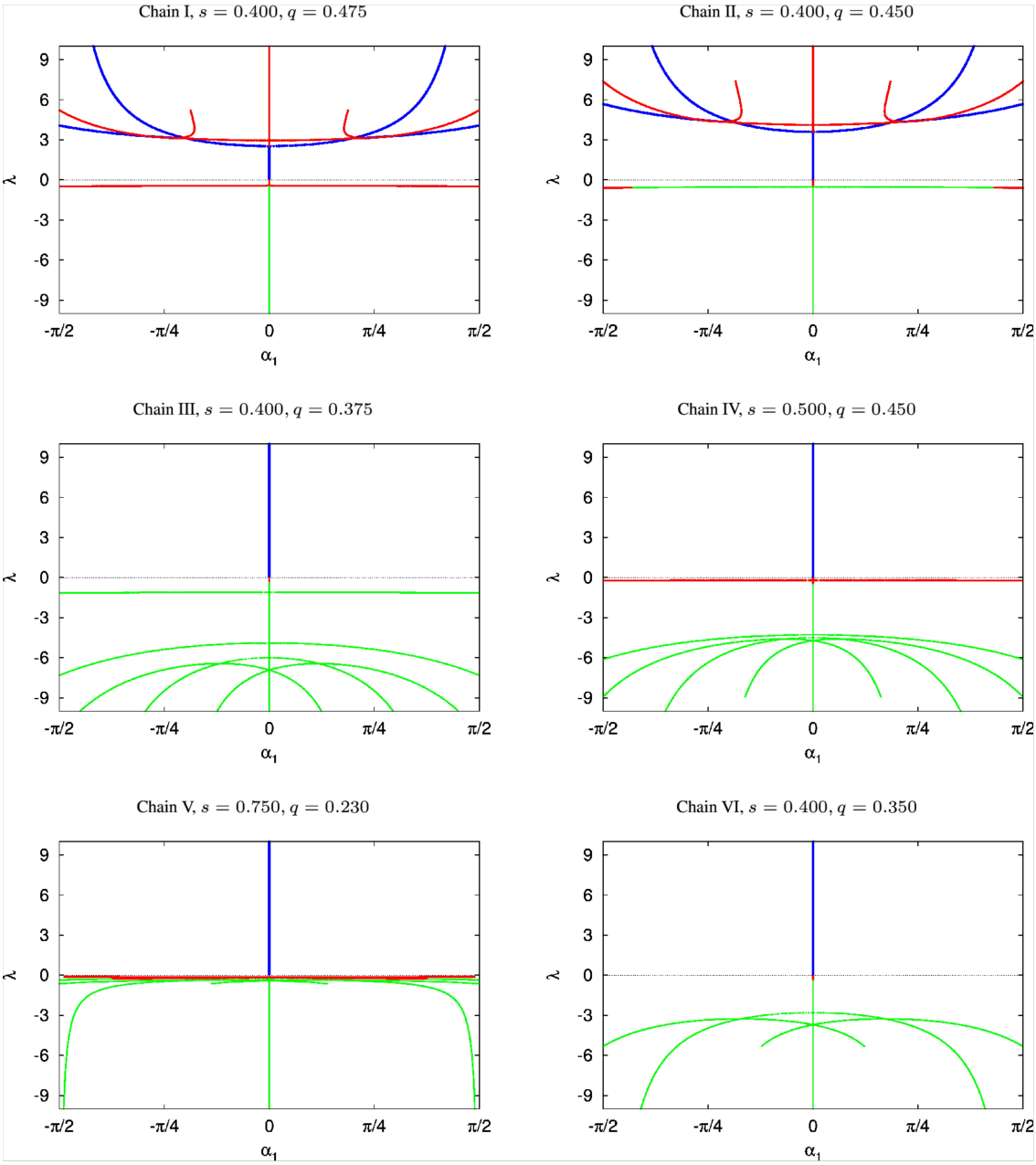

Figure 3: Projections of the equilibrium paths on the subspace of the load parameter λ and plate rotation α^1. Blue and red colors represent stable and unstable equilibrium states, respectively, while green denotes physically inadmissible states. (λ is positive in tension.)

The diagram for Chain III shows three physically inadmissible bifurcations under compression. In this projection there seems to be another bifurcation on the trivial path for larger compression. However, only symmetric bifurcations can occur from the trivial path, due to the mirror symmetry of the equilibrium configurations to the *Y*-axis. Hence, the paths that seem to cross the trivial path below λ<-6 are separated from it in the full 4D GRS. Instead, these paths bifurcate from that secondary branch which corresponds to pure shear buckling. It will be seen in 3D plots.

The diagram for Chain IV reveals three bifurcations under compression, one of them, a mixed buckling mode, is physically admissible. Besides, this diagram is fairly similar to the previous one.

In the diagram for Chain V, three bifurcations can be seen under compression. Two of them, the mixed buckling modes, are physically admissible. These bifurcations are difficult to observe in the proximity of the trivial path, but at around $\alpha^1=\pi/2$, the three secondary paths can be clearly seen. Note that one stable secondary path becomes physically inadmissible for larger values of the plate rotation α^1. There are also two, physically inadmissible paths. They branch from the secondary path of pure shear buckling, and do not cross the trivial equilibrium path in the whole 4D GRS.

The diagram for Chain VI shows one physically inadmissible bifurcation under compression, which belongs to pure shear buckling. The bifurcations for mixed buckling modes disappeared. Besides, there are two tertiary paths, that branch from the single secondary path.

Next, we show the projections of the equilibrium paths on the 3D subspace $(\alpha^1, \alpha^2, \lambda)$ of the GRS. See Figure 4 for the studied six stiffness parameter pairs. In these diagrams the paths are also projected on the subspaces (α^2, λ) and (α^1, α^2), and plotted in gray.

In the diagrams for Chains I and II, we can see that the two higher order branches are bifurcated from the unstable secondary path under tension. The stability of the secondary path changes at these bifurcations. Note that on the stable secondary branch $\alpha^1=\alpha^2$ holds. These two diagrams are very similar, the only major difference is that the lowest secondary branch is shifted down and it gets into the physically inadmissible regime. In the diagram for Chain III, we can see the three, physically inadmissible secondary paths and the two, physically inadmissible tertiary paths. The equilibrium paths get higher and the topmost secondary path becomes physically admissible in the diagram for Chain IV. Then in the diagram for Chain V, the paths are more elevated, and the secondary branch in the middle also becomes physically admissible. Note that the projections of the secondary paths on (α^1, α^2) are similar in the diagrams for Chains III–V. In the diagram for Chain VI, two secondary paths disappeared, only a physically inadmissible secondary path and its branching tertiary paths can be seen.

Now, the projections of the equilibrium paths on the 3D subspace $(\alpha^1, \alpha^3, \lambda)$ are shown in Figure 5 for the studied six stiffness parameter pairs. In these diagrams the paths are also projected on the subspaces (α^3, λ) and (α^1, α^3), and plotted in gray. Here we can make some further observations.

First, the stable secondary paths for Chains I and II, and the lowest secondary path for Chains III–VI obey $\alpha^1=\alpha^3$. (See the projections on the horizontal plane.) For these paths $\alpha^1=\alpha^2$ holds according to Figure 4. Therefore, these are the equilibrium paths that belong to pure shear buckling, as already expected from the analytical results.

Second, the tertiary paths for Chains I and II are connected to the unstable secondary path of mixed buckling modes under tension, while the tertiary paths for Chains III–VI are connected to the secondary path of pure shear buckling. Then, in a topological point of view, the (shown part of the) bifurcation diagrams for Chains I and II are topologically equivalent, and the (shown part of the) bifurcation diagrams for Chains III–V are topologically equivalent. For the explanation of this observation we have to get back to Figure 2, where the relevant triangle of the parameter plane is shown. This triangle is divided into three parts by line $s=q$ and curve $d=0$. These are the main partitions of the parameter plane of a stretched chain of three plates. If we have several chains with different stiffness properties, but they are represented in the same main partition of the parameter plane, then we can suspect that these chains have topologically equivalent bifurcation diagrams. Although, the physical admissibility of the paths can vary.

This observation may be generalized for longer chains as well. According to [9], the parameter plane, (s,q), of a chain of N+1 plates can be divided into N+1 main partitions. Hence, it is conjectured that a pinned–stretched, straight, linear elastic discrete *Cosserat* rod of N+1 plates can lead to N+1 types of bifurcation diagrams, which are topologically not equivalent. The values of the two stiffness parameters of the chain determine that which type of bifurcation diagram the structure possesses.

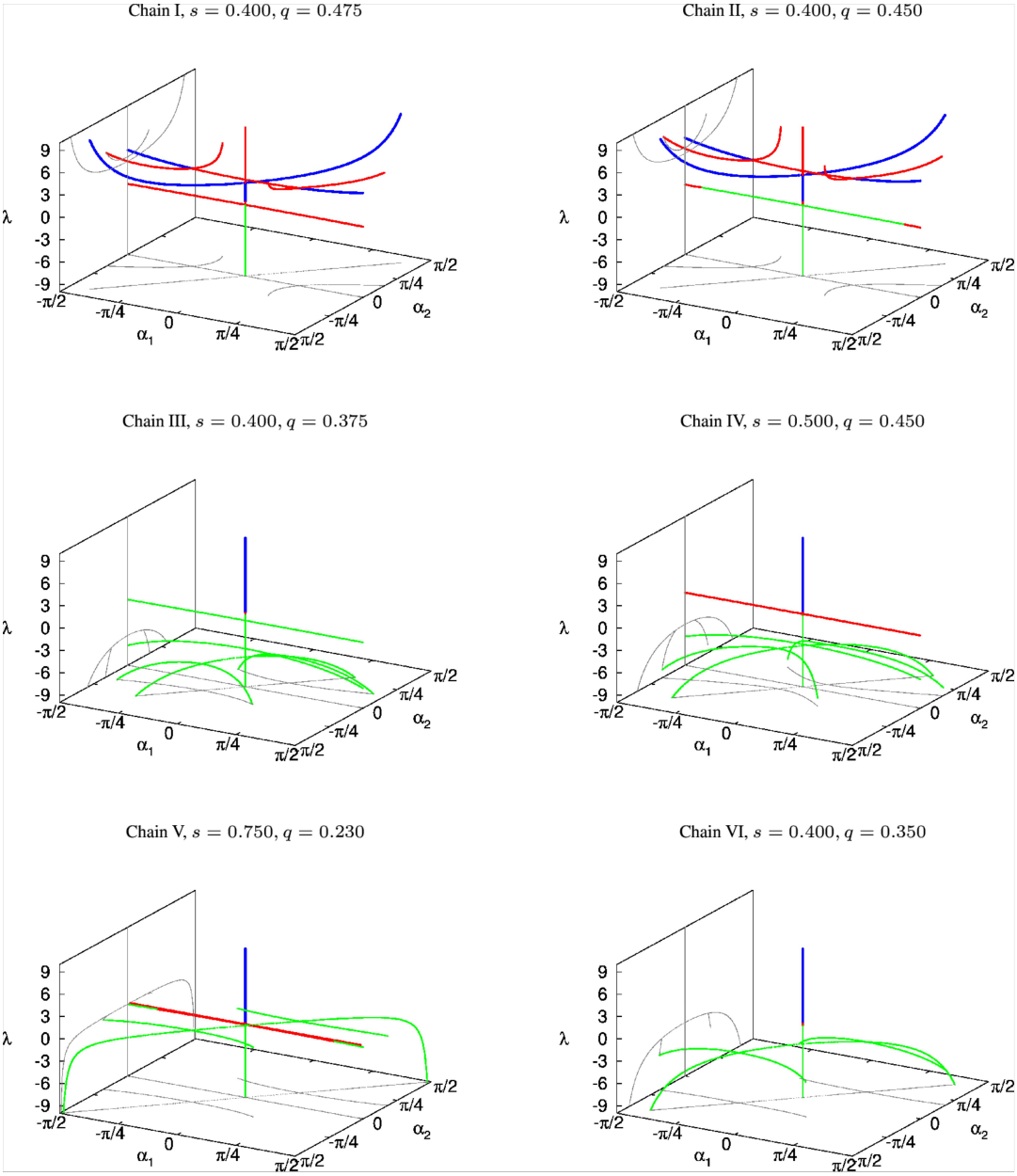

Figure 4: 3D plots of the equilibrium paths: load parameter λ vs plate rotations α^1 and α^2. Blue and red colors represent stable and unstable equilibrium states, respectively, while green denotes physically inadmissible states. Projections of the paths on the subspaces (α^2, λ) and (α^1, α^2) are gray.

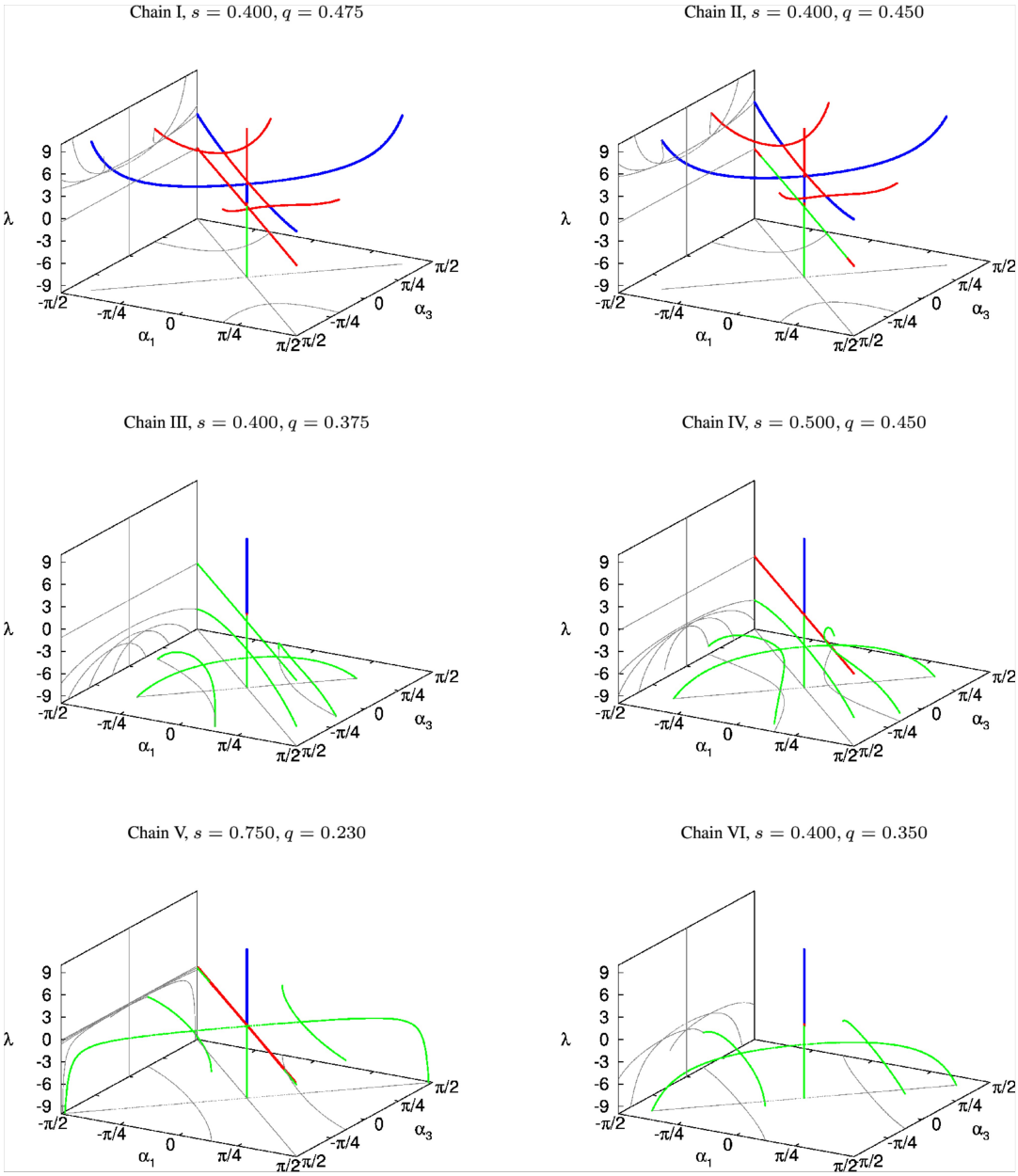

Figure 5: 3D plots of the equilibrium paths: load parameter λ vs plate rotations α^1 and α^3. Blue and red colors represent stable and unstable equilibrium states, respectively, while green denotes physically inadmissible states. Projections of the paths on the subspaces (α^3, λ) and (α^1, α^3) are gray.

4 CONCLUSIONS

In this paper we dealt with a discrete model of the planar *Cosserat* rod. First, we reviewed the equilibrium equations and the buckling loads of a pinned–stretched rod based on [9], considering straight, stress–free state and identical linear elastic material in each segment. Then we started some new investigations. We accomplished a global numerical analysis to compute the equilibrium states of a chain of three plates. The plane, spanned by the two independent stiffness parameters of the chain, can be partitioned into six parts. Each of these six parts of the parameter plane represents a qualitatively different mechanical behavior of the structure. A stiffness parameter pair was chosen from each unique part of the parameter plane and chains equipped with these material properties were studied further. We showed that the solutions of the equilibrium equations formed equilibrium paths, uniquely embedded in a 4D

General Representation Space (GRS). These equilibrium paths were calculated for large displacements with the Simplex Scanning Algorithm, within a bounded domain of the GRS. The results were refined by a NR iteration, and the stability of the equilibrium states were also determined. The numerical results were verified with the analytical buckling loads of the studied chains. Projections of the calculated equilibrium paths on 2D and 3D subspaces were shown for all the six studied stiffness parameter pairs. In these plots, stable, unstable and physically inadmissible states were indicated. The simplest buckling mode of the model, the pure shear buckling was identified numerically in each case. This buckling mode occurs under tensile load if the chain is softer for shearing than for tension. In this case, the secondary equilibrium path of the pure shear buckling is stable, and it has no tertiary branches. However, the unstable secondary path, which belongs to a mixed buckling mode under tension, has further bifurcations. Pure shear buckling occurs under compression if the chain is softer for tension than for shearing. In this case the secondary equilibrium path of the pure shear buckling is physically inadmissible, and tertiary branches bifurcate from it. Isolated equilibrium paths have not been found in the studied domain of the GRS.

The studied discrete model can be used to analyze rod–like engineering structures with finite shear, normal and bending stiffness, especially if they have a discrete macroscopic nature, but it can also be useful in modeling macromolecules, such as DNA, or nanobeams.

ACKNOWLEDGEMENT

This paper was supported by the János Bolyai Research Scholarship of the Hungarian Academy of Sciences and by OTKA No. PD 100786.

REFERENCES

[1] Timoshenko S. P. and Gere J., *Theory of elastic stability*. McGraw–Hill, New York, 1961.

[2] Antman S. S., *Nonlinear problems of elasticity*. Springer, New York, 2005.

[3] Coleman B. D., Olson W. K., and Swigon D., "Theory of sequence–dependent DNA elasticity", *Journal of Chemical Physics*, **118**:7127–7140, 2003.

[4] Challamel N., Wang C. M., and Elishakoff I., "Discrete systems behave as nonlocal structural elements: Bending, buckling and vibration analysis", *European Journal of Mechanics - A*, **44**:125–135, 2014.

[5] Hencky H., "Über die angenäherte Lösung von Stabilitätsproblemen im Raummittels der elastischen Gelenkkette", *Der Eisenbau*, **11**:437–452, 1920. In German.

[6] Kocsis A., Németh R. K., and Károlyi Gy., "Spatially chaotic bifurcations of an elastic web of links", *International Journal of Bifurcation and Chaos*, **20**:4011–4028, 2011.

[7] Németh R. K. and Kocsis A., "Bielastic web of links: a discrete model of Csonka's beam", *International Journal of Non-Linear Mechanics*, **63**:49–59, 2014.

[8] Csonka P., "Buckling of bars elastically built–in along their entire length", *Acta Technica Hungarica,* **32:**423–427, 1961.

[9] Kocsis A., "Buckling analysis of the discrete planar cosserat rod", *International Journal of Structural Stability and Dynamics*, **16**(1):1450111/1–29, 2016.

[10] Gáspár Zs., Domokos G., and Szeberényi I., "A parallel algorithm for the global computation of elastic bar structures", *Computer Assisted Mechanics and Engineering Sciences*, 4:55–68, 1997.

[11] Love A. E. H., *A treatise on the mathematical theory of elasticity (4th ed.)*. Dover Publications, New York, 1944.

[12] Zhang Z., Challamel N., and Wang C. M., “Eringen's small length scale coefficient for buckling of nonlocal timoshenko beam based on microstructured beam model”, *Journal of Applied Physics*, **114**:114902/1–6, 2013.

[13] Bažant Z. P. and Cedolin L., *Stability of Structures – Elastic, Inelastic, Fracture and Damage Theories*, Oxford University Press, New York, 1991.